Title

Correlating structural and photochemical heterogeneity in cyanobacteriochrome NpR6012g4

Journal

Proceedings of the National Academy of Sciences of the United States of America, 115(17)

ISSN

0027-8424

Authors

Lim, Sunghyuk
Yu, Qinhong
Gottlieb, Sean M
et al.

Publication Date

2018-04-24

DOI

10.1073/pnas.1720682115

Peer reviewed

Correlating structural and photochemical heterogeneity in cyanobacteriochrome NpR6012g4

Sunghyuk Lim[a,1], Qinhong Yu[a,1], Sean M. Gottlieb[a,2], Che-Wei Chang[a,3], Nathan C. Rockwell[b], Shelley S. Martin[b], Dorte Madsen[a], J. Clark Lagarias[b,4], Delmar S. Larsen[a,4], and James B. Ames[a,4]

[a]Department of Chemistry, University of California, Davis, CA 95616; and [b]Department of Molecular and Cellular Biology, University of California, Davis, CA 95616

Contributed by J. Clark Lagarias, March 20, 2018 (sent for review November 28, 2017; reviewed by Kevin H. Gardner, John T. M. Kennis, and Keith Moffat)

Phytochrome photoreceptors control plant growth, development, and the shade avoidance response that limits crop yield in high-density agricultural plantings. Cyanobacteriochromes (CBCRs) are distantly related photosensory proteins that control cyanobacterial metabolism and behavior in response to light. Photoreceptors in both families reversibly photoconvert between two photostates via photoisomerization of linear tetrapyrrole (bilin) chromophores. Spectroscopic and biochemical studies have demonstrated heterogeneity in both photostates, but the structural basis for such heterogeneity remains unclear. We report solution NMR structures for both photostates of the red/green CBCR NpR6012g4 from *Nostoc punctiforme*. In addition to identifying structural changes accompanying photoconversion, these structures reveal structural heterogeneity for residues Trp655 and Asp657 in the red-absorbing NpR6012g4 dark state, yielding two distinct environments for the phycocyanobilin chromophore. We use site-directed mutagenesis and fluorescence and absorbance spectroscopy to assign an orange-absorbing population in the NpR6012g4 dark state to the minority configuration for Asp657. This population does not undergo full, productive photoconversion, as shown by time-resolved spectroscopy and absorption spectroscopy at cryogenic temperature. Our studies thus elucidate the spectral and photochemical consequences of structural heterogeneity in a member of the phytochrome superfamily, insights that should inform efforts to improve photochemical or fluorescence quantum yields in the phytochrome superfamily.

biliprotein | light sensor | photoswitch | photoacclimation | optogenetics

Providing reliable food sources in the face of climate change and expanding populations requires substantial improvements in food production (1). Modern agriculture relies on high planting densities of photosynthetic plants, but such densities cause competition among individual plants for light and trigger the shade avoidance response, reducing overall crop yield (2). Shade avoidance responses are controlled by plant phytochromes, large (≥1,100 aa) photoreceptors that reversibly photoconvert between red- and far-red–absorbing photostates to act as master regulators for light-dependent plant development [photomorphogenesis (3–5)]. Improvements in agricultural performance are thus linked to our ability to redirect the phytochrome shade avoidance response in crop plants.

Phytochromes are also found in diverse bacteria, eukaryotic algae, and fungi (6, 7), sharing a conserved three-domain photosensory core module (PCM) (8–11) that binds a covalently attached linear tetrapyrrole (bilin) chromophore. Photoisomerization of the bilin 15,16-double bond allows phytochromes to reversibly photoconvert between two photostates having distinct spectral and biochemical properties with a photochemical quantum yield below 30% (3, 12–15). Phytochromes also exhibit several types of heterogeneity. Known structural heterogeneity includes differences in side-chain rotamers and protonation state (16, 17). Known spectral heterogeneity includes the presence of populations with different peak wavelengths and fluorescence properties (14, 18–20). Spectrally similar phytochrome populations can also exhibit photochemical heterogeneity by having different excited-state lifetimes and quantum yields (12–14). Plant phytochromes also reveal biological heterogeneity, because different populations have different signaling activity within a single photostate (21). The connections between these types of heterogeneity are not well understood, but biological heterogeneity has important consequences for phytochrome function: maximal signaling activity in plant phytochrome A occurs in a population of the red-absorbing dark state generated by photoconversion (21), so the low quantum yield of phytochrome and the presence of other populations limit maximal signaling. Available crystal structures do not elucidate the structural basis for any facet of phytochrome heterogeneity. Solid-state NMR has allowed modeling of heterogeneity in a cyanobacterial phytochrome (17, 22) but does not provide atomic resolution, and the complete phytochrome PCM is too large for structure determination via conventional solution NMR spectroscopy (23).

Fortunately, the phytochrome superfamily also includes cyanobacteriochromes (CBCRs), a spectrally diverse family of cyanobacterial photoreceptors. CBCRs control various aspects of cyanobacterial photobiology (24–27) and exhibit a plethora of

Significance

Photosynthetic organisms measure changing light conditions with photosensory proteins. In land plants, phytochromes use the ratio of red to far-red light to detect shading by neighboring plants. Cyanobacteria use distantly related cyanobacteriochromes (CBCRs) to detect a broad range of conditions so that they can optimize light harvesting, movement, and other photobiology. Both phytochromes and CBCRs naturally occur as heterogeneous mixtures of populations, but the links between structural and photochemical heterogeneity are unclear. We have solved the structure of a model CBCR in both photostates, allowing us to explicitly connect structural heterogeneity of conserved residues to populations having distinct spectral and photochemical properties.

Author contributions: N.C.R., J.C.L., D.S.L., and J.B.A. designed research; S.L., Q.Y., S.M.G., C.-W.C., N.C.R., S.S.M., and J.B.A. performed research; S.L., Q.Y., N.C.R., D.M., J.C.L., D.S.L., and J.B.A. analyzed data; and S.L., Q.Y., N.C.R., J.C.L., D.S.L., and J.B.A. wrote the paper.

Reviewers: K.H.G., City University of New York Advanced Science Research Center; J.T.M.K., Vrije Universiteit Amsterdam; and K.M., The University of Chicago.

The authors declare no conflict of interest.

Data deposition: The atomic coordinates and structure factors have been deposited in the Protein Data Bank, www.wwpdb.org [PDB ID codes 6BHN (dark state) and 6BHO (photoproduct)].

[1]S.L. and Q.Y. contributed equally to this work.

[2]Present address: Department of Life/Physical Sciences, Allan Hancock College, Santa Maria, CA 93454.

[3]Present address: Department of Pathology and Laboratory Medicine, University of California, Davis, Sacramento, CA 95817.

[4]To whom correspondence may be addressed. Email: jclagarias@ucdavis.edu, dlarsen@ucdavis.edu, or jbames@ucdavis.edu.

This article contains supporting information online at www.pnas.org/lookup/suppl/doi:10.1073/pnas.1720682115/-/DCSupplemental.

Published online April 9, 2018.

photocycles (6, 26, 28–31). Red/green CBCRs such as AnPixJg2 and slr1393g3 exhibit a red-absorbing dark state similar to that of plant phytochrome but are much smaller (6, 32, 33). Crystal structures demonstrate that the PCB chromophore adopts a C5-*Z,syn* C10-*Z,syn* C15-*Z,anti* geometry in the red-sensing state, as in phytochrome (8, 9, 11, 34). AnPixJg2 and slr1393g3 exhibit structural heterogeneity at residues distant from the chromophore, but detailed characterization of spectral or photochemical heterogeneity in these two proteins has not been reported. AnPixJg2 is closely related to NpR6012g4 from *Nostoc punctiforme* (35), which has been shown to be photochemically heterogeneous on the ultrafast timescale (36–39). NpR6012g4 has also been characterized using solution NMR, with complete chromophore chemical shift assignments and secondary structure already reported for both photostates (40–43).

We here report atomic-resolution solution structures for NpR6012g4 in both photostates. The photoproduct state resembles that of slr1393g3 [Protein Data Bank (PDB) ID code 5M82], whereas the dark state reveals unexpected structural heterogeneity at key residues close to the PCB chromophore. Thus, the protein matrix surrounding the bilin is heterogeneous in red/green CBCRs despite an apparently homogenous chromophore at the level of NMR spectroscopy (40, 41, 44, 45). Comparison of NpR6012g4 variants with the observed heterogeneity of Trp655 predicts the existence of an orange-absorbing population in the wild-type dark state. We confirm this predicted spectral heterogeneity using absorption and fluorescence excitation spectroscopy and demonstrate that the orange-absorbing population does not give rise to the photoproduct. Based on pH responses in both wild-type and variant NpR6012g4, we propose that loss of hydrogen bonds between PCB and the structurally heterogeneous Asp657 causes the spectral shift in this photochemically inactive population. This work thus explicitly links structural heterogeneity at specific residues to spectral and photochemical heterogeneity in a member of the phytochrome superfamily.

Results

Determination of Solution Structures for both Photostates of NpR6012g4. We previously reported secondary-structure assignments (Biological Magnetic Resonance Bank accession numbers 26577 and 26582) and chromophore chemical shifts for NpR6012g4 in both photostates (40–43). We used these assignments to derive structural restraints and perform high-resolution structural analysis of both photostates. Atomic-level structures were calculated using distance restraints derived from nuclear Overhauser effect (NOE) cross-peaks (Fig. S1) and long-range orientational restraints derived from residual dipolar coupling (46) data (Fig. S2). The first 16 and last 8 residues in NpR6012g4 were dynamically disordered and are absent from the final structural ensembles, so NMR structures were resolved for 155 aa from Ser599 to Val754 using numbering for the full-length protein (GenBank accession number Npun_R6012). The 10 lowest-energy NMR structures for the red-absorbing dark state and green-absorbing photoproduct are shown in Fig. 1 *A* and *B*, with structural statistics summarized in Table S1. We obtained an rmsd of 0.61 Å (dark state) and 0.67 Å (photoproduct) for main-chain coordinates. Energy-minimized average structures for each state calculated from the ensembles in Fig. 1 have the expected GAF domain topology (Fig. S3*A*) with a six-stranded antiparallel β-sheet (β1, R620–F626; β2, V635–A640; β3, K645–V647; β4, N673–V676; β5, A699–A707; β6, Q710–Q719) flanked by four α-helices (α2, V601–L616; α3, H659–A669; α4, H688–Q694; α5, E728–Q747). The average NMR structures of the two NpR6012g4 photostates have an overall rmsd of 2.5 Å, and the average structure of the dark state is quite similar to the crystal structure of the red-absorbing dark state of AnPixJ (rmsd, 1.5 Å) except for the absence of the N-terminal helix and the presence of a shorter C-terminal helix. Photoconversion induces migration of a short stretch of residues around Trp655. In the dark state, the Trp655 indole ring forms a π-stacking interaction with the PCB D-ring, and the indole NH is hydrogen bonded to the A-ring carbonyl oxygen (Fig. 1*C*). Upon photoconversion, both of these protein–chromophore interactions are lost (Fig. 1*D*). The indole ring is instead extruded toward bulk solvent and is now close to the C3 side chain on the A-ring, consistent with a similar migration observed in crystal structures of slr1393g3 (PDB ID code 5M82).

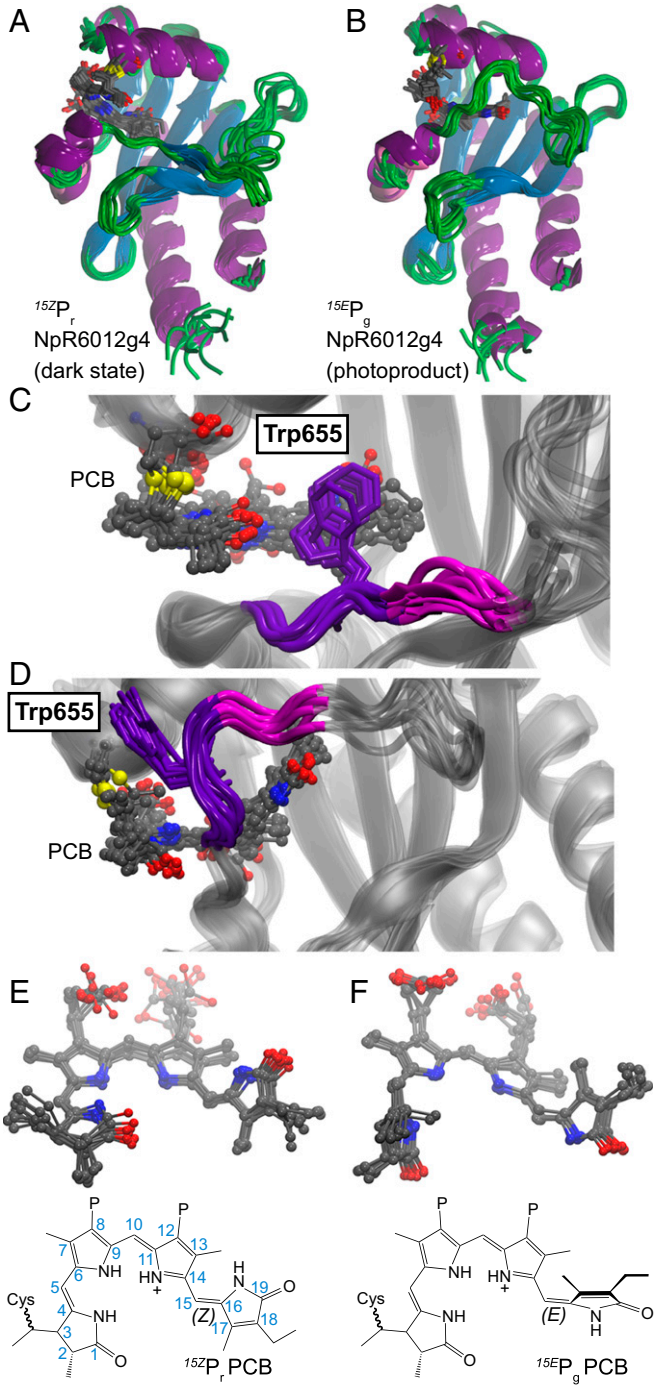

Fig. 1. Solution structures of NpR6012g4. (*A*) The ensemble of solution structures is shown for the red-absorbing dark state (α-helix, purple; β-strand, cyan; other, green). PCB chromophore and the covalently attached Cys687 are indicated in stick view (gray, carbon; blue, nitrogen; red, oxygen; yellow, sulfur). PDB ID code 6BHN. (*B*) The ensemble of solution structures is shown for the green-absorbing photoproduct as in *A*. PDB ID code 6BHO. (*C*) Trp655 is shown packed onto PCB in the dark state, with residues 653–654 and 655–657 highlighted in pink and purple, respectively. (*D*) The same region is shown in the photoproduct. (*E*) The 15*Z* PCB chromophore of the dark state is shown in the ensemble (*Top*) and as a schematic (*Bottom*; P, propionate). (*F*) The 15*E* PCB chromophore of the photoproduct is shown as in *E*.

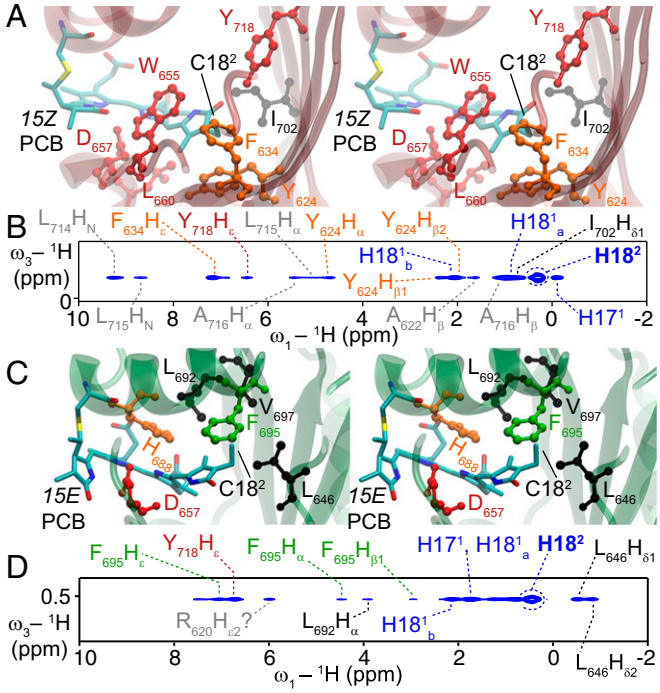

Fig. 2. Protein–chromophore interactions around the photoactive D-ring of NpR6012g4. (*A*) Representative stereoview of the PCB-binding pocket of the NpR6012g4 dark state (*Top*). Heavy atoms of PCB chromophore and covalently attached Cys687 are shown in stick view and colored by atom type (C, cyan; N, blue; O, red; S, yellow). Residues within 3.1 Å of the PCB D-ring and/or C15 methine bridge (see text) are shown in ball-and-stick view and are color-coded by phenotype as discussed in the text (red, effects on the dark state; green, effects on the photoproduct; orange, effects on both; black, no significant effects). (*B*) Nuclear Overhauser effect (NOE) cross-peaks are shown for the $H18^2$ methyl carbon of PCB in the dark state. Residues within 3.1 Å of the D-ring follow the color code of *A*; other amino acids are indicated in gray, and PCB cross-peaks are indicated in blue. (*C*) A representative stereoview is shown for the PCB-binding pocket of the NpR6012g4 photoproduct as in *A*. (*D*) Nuclear Overhauser effect (NOE) cross-peaks are shown for the $H18^2$ methyl carbon of PCB in the photoproduct as in *B*.

Protein–Chromophore Interactions in NpR6012g4. In the dark state, the PCB chromophore of NpR6012g4 adopts the expected C5-*Z*, *syn* C10-*Z,syn* C15-*Z,anti* configuration (Fig. 1*E*) seen in the red-absorbing states of AnPixJg2 and phytochromes (8, 9, 11, 34). The A-ring and D-ring adopt α-facial dispositions relative to the approximate plane defined by the B- and C-rings (47). The 8-propionate is well ordered, but the 12-propionate adopts several conformations (Fig. S3*B*). Photoconversion results in photoisomerization of the 15,16-double bond to the 15*E* configuration (Fig. 1 *E* and *F*) and rotation of the chromophore within the chromophore-binding pocket (Fig. S3*C*), reminiscent of the flip-and-rotate model proposed for phytochromes (48). The PCB D-ring remains on the α face of the bilin, but the A-ring moves from the α face to the β face while retaining the C5-*Z,syn* configuration (Fig. 1*F*). Movement of the A-ring arises due to approximate inversion of the dihedral angle for the 5,6-single bond (Table S2). The photoproduct chromophore exhibits increased tilt of the A-ring relative to the B-ring, more modest increases in B/C ring tilt and C/D ring tilt (Table S2), and increased disorder of the 8-propionate (Fig. S3*D*). The C17-methyl group is within 5 Å of both the C15 methine proton and the C13 methyl group, in keeping with intramolecular NOE cross-peaks specifically observed in the photoproduct state (40). Overall, the photoproduct chromophore is more twisted than that of the dark state, which should result in weaker conjugation of the bilin π system consistent with the blue-shifted photoproduct absorbance.

Some protein–chromophore interactions are retained upon photoconversion, whereas others change. His659 is proximal to the bilin C10 atom in both photostates (Table S2), consistent with the ability of $H_{659}C$ NpR6012g4 to form a second linkage to the chromophore at C10 (35). In the dark state, the 8-propionate forms hydrogen bonds to His688 (10 out of 10 structures), Ser685 (7/10), and His684 (1/10). Upon photoconversion, hydrogen bonds from the 8-propionate to these three residues are still present (9/10, 9/10, and 1/10, respectively). By contrast, the 12-propionate is hydrogen bonded to Arg667 (6/10), His659 (2/10), His684 (1/10), and Tyr668 (1/10) in the dark state but to Tyr668 (7/10) and Tyr700 (9/10) in the photoproduct. There are also changes in the vicinity of the photoactive D-ring. In the dark state, the D-ring and/or C15 methine bridge are within 3.1 Å of Tyr624, Phe634, Trp655, Asp657, Leu660, Ile702, and Tyr718 in eight or more structures (Fig. 2 *A* and *B*). In the photoproduct, the D-ring and/or 15-methine bridge are within 3.1 Å of Leu646, Asp657, His688, Leu692, Phe695, and Val697 in eight or more structures (Fig. 2 *C* and *D*).

A Photochemically Inert Orange-Absorbing Population in the NpR6012g4 Dark State. Substitutions for Trp655 have given varying results (15). $W_{655}V$ and $W_{655}A$ variants both exhibited spectrally heterogeneous 15*Z* dark states containing both red- and orange-absorbing populations, but $W_{655}H$ NpR6012g4 failed to bind chromophore (15). The equivalent Trp289 adopted multiple conformations in a microsecond simulation of the AnPixJg2 dark state (49), so this

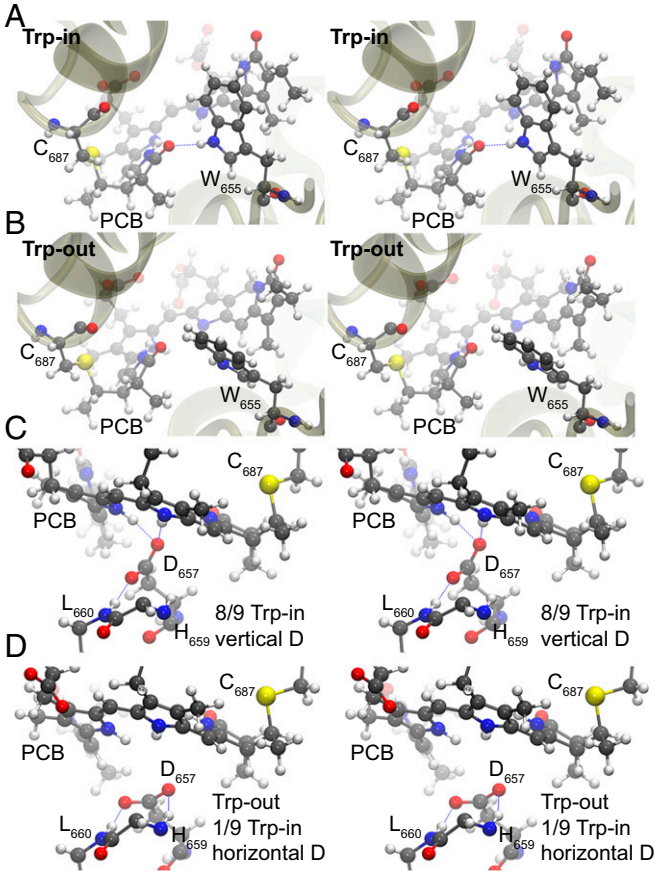

Fig. 3. Heterogeneity at Trp655 and Asp657 in the NpR6012g4 dark state. (*A*) Stereoviews are shown for a representative Trp-in configuration of Trp655. (*B*) Stereoviews are shown for the Trp-out configuration. (*C*) Stereoviews are shown for a representative vertical configuration of Asp657, with hydrogen bonds indicated. (*D*) Stereoviews are shown for a representative horizontal configuration of Asp657.

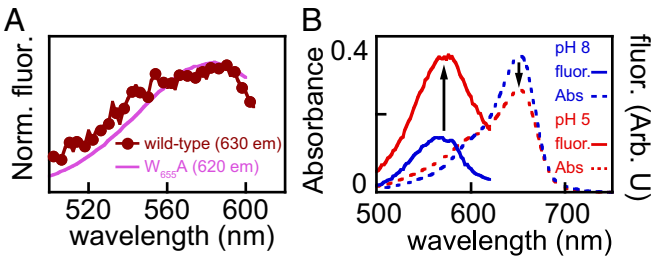

Fig. 4. Spectroscopic analysis of NpR6012g4 heterogeneity. (*A*) Normalized fluorescence excitation spectra are shown for wild-type (λ_{em}, 630 nm; brick red) and $W_{655}A$ (λ_{em}, 620 nm; dusty rose) NpR6012g4. (*B*) Absorption (dotted) and fluorescence excitation (λ_{em}, 640 nm; solid) spectra are shown for wild-type NpR6012g4 at pH 5 (red) and pH 8 (dark blue). Arrows indicate direction of change with lower pH.

variation could be explained by structural heterogeneity of this Trp. Remarkably, we observed structural heterogeneity at Trp655 in the NpR6012g4 dark-state ensemble. The π-stacked orientation (hereafter, "Trp-in") was present in 9 out of 10 structures (Figs. 1*C* and 3*A*). The other structure instead exhibited a Trp-out orientation in which the Trp side chain was rotated away from the D-ring about the χ2 angle (Fig. S3*E*), disrupting both π stacking and the hydrogen bond between Trp655 and the PCB A-ring (Fig. 3*B*). The Trp-out configuration was seen in ∼10% of the structures in multiple independent ensembles, even though the region from Trp655 to Asp657 was well ordered (Fig. 1*C*). The side-chain Nε1 atom of Trp655 exhibited modest but significant reductions in heteronuclear NOE (hetNOE) and T_1/T_2 ratio in the dark state compared with the backbone N atoms of residues 655–657 but not compared with those of the more mobile Thr653 and Val654 (Fig. S3*F*). Such differences were not observed in the photoproduct (Fig. S3*G*). We thus conclude that Trp655 is a site of structural heterogeneity in the NpR6012g4 dark state, with a minority population adopting the Trp-out configuration.

$W_{655}V$ and $W_{655}A$ variants accumulate 15*Z* orange-absorbing species (15), so we reasoned that the Trp-out population in wild-type NpR6012g4 could absorb orange light. Such a population is not seen in the wild-type absorption spectrum, but we confirmed its presence using fluorescence excitation spectroscopy (Fig. 4*A*). Moreover, the excitation spectrum for this species was similar to that for the orange-absorbing population of $W_{655}A$ NpR6012g4 (Fig. 4*A*), implicating a common chromophore environment for orange-absorbing species in both wild-type and variant NpR6012g4 proteins. These results confirm the presence of spectral heterogeneity in the NpR6012g4 dark state.

We next sought to enrich the orange-absorbing population in wild-type NpR6012g4 to examine photochemical consequences of spectral heterogeneity. Unlike wild-type NpR6012g4, the $W_{655}V$ variant exhibited increased orange absorption with decreasing temperature (Fig. S4 *A* and *B*). We reasoned that a similar process might occur in wild-type NpR6012g4 at cryogenic temperatures. Indeed, we observed that rapid cooling of dark-state NpR6012g4 to 150 K resulted in retention of red absorbance, whereas slow cooling resulted in formation of substantial orange absorbance (Fig. 5*A*). We illuminated the slow-cooled preparation with orange or green light and then compared the resulting difference spectra for primary photoconversion to that obtained upon illumination of the fast-cooled preparation with red light (Fig. 5 *A* and *B*). Illumination of slow-cooled NpR6012g4 with orange or green light should preferentially excite the orange-absorbing species, but all three conditions gave near-identical difference spectra (Fig. 5*B*). Therefore, preferential excitation of the orange-absorbing species did not result in formation of distinct photoproducts at 150 K.

To examine potential reactivity of the orange-absorbing species at physiologically relevant temperatures, we used time-resolved spectroscopy. Previous work had shown that robust signals could be obtained with 532-nm excitation of NpR6012g4 on a timescale of nanoseconds to milliseconds (50), so we used this approach for comparison with previously reported ultrafast spectroscopy (picoseconds to nanoseconds) using 650-nm excitation (38). In this experiment, 532-nm excitation preferentially enhances excitation of the orange-absorbing population (Fig. 5*C*), and early secondary spectra (<10 ns) showed enhanced negative bleach at 590 nm compared with the bleach at 650 nm (Fig. S5 *A*–*D*). Consistent with measurements at 150 K, a single positive band was observed at 680 nm regardless of excitation wavelength (Fig. S5 *A* and *B*). The bleach at 590 nm decayed much more rapidly than that at 650 nm (∼20 ns and 1 μs, respectively), but the positive band at 680 nm decayed on both timescales (Fig. S5*C*). This difference was also observed in the two bleach amplitudes at 2 ns – 200 ns (Fig. S5*A*): bleach at 590 nm decayed, but that at 650 nm did not.

We conclude that 532-nm excitation generated Lumi-O_f and Lumi-R_f primary photoproducts from the orange- and red-absorbing populations, respectively; the two photoproducts exhibited similar positive absorption but different bleaches and decay kinetics. We used the large difference in decay timescales of these intermediates to estimate the Lumi-O_f spectrum by subtracting the raw 10-ns spectrum from that at 2 ns (Fig. S5*E*, orange trace), revealing a positive absorption resembling the positive absorption of Lumi-R_f under 650-nm excitation (Fig. S5*B*). Two other transitions were also clear from the raw signals (Fig. S5 *A*–*D*): evolution of the primary photoproduct absorption into a Meta-R_y intermediate peaking at 570 nm and subsequent appearance of a Meta-R_g intermediate peaking at ∼550 nm. Difference spectra for these transitions could be approximated using 1-μs and 200-ns spectra for Meta-R_y and 1-ms and 500-μs spectra for Meta-R_g (Fig. S5*E*, red and green circles, respectively).

The amplitude of the positive 575-nm band for Meta-R_y formation is comparable to that of the negative 650-nm band for Lumi-R_f decay (compare 200-ns and 1-μs spectra, Fig. S5*A*). Assuming comparable extinction coefficients for the two primary photoproducts, which is plausible given their similar properties, we can therefore estimate the amplitude of Lumi-O_f in the transient absorption (TA) signals as equal to or greater than that of Lumi-R_f using the decay at 680 nm (Fig. S5 *A* and *C*).

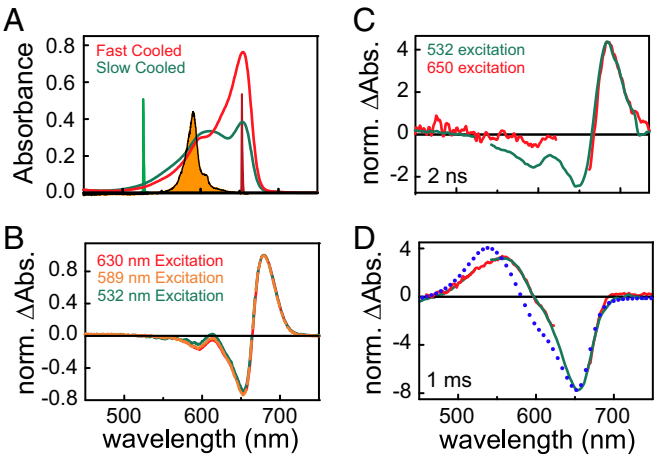

Fig. 5. The orange-absorbing population in the NpR6012g4 dark state does not undergo full photoconversion. (*A*) Absorption spectra are shown for 15*Z* NpR6012g4 at 150 K after fast (red) or slow (green) cooling. Sources for red (630 nm), orange (589 nm), and green (532 nm) excitation are indicated. (*B*) Difference spectra are shown for illumination of slow-cooled NpR6012g4 at 150 K with green (green) or orange (orange) light and of fast-cooled NpR6012g4 with red light (red). (*C*) Difference spectra are shown for NpR6012g4 2 ns after excitation with 532-nm light (green) or 630-nm light (red). (*D*) Difference spectra are shown for NpR6012g4 1 ms after illumination with the same sources as in *C*. The difference spectrum for photoconversion of NpR6012g4 under static illumination (blue circles) is shown for comparison.

Were Lumi-O_f to generate a subsequent photoproduct, this species would be readily detectable before decay of Lumi-R_f. However, Meta-R_y did not appear on this timescale (e.g., 50-ns trace: Fig. S5*A*); instead, the additional bleach observed at 590 nm decayed without appearance of additional intermediates (Fig. 5 *A* and *C*).

We next constructed a global target model to analyze the secondary dynamics of NpR6012g4 (Fig. S6). We postulated parallel excitation of red- and orange-absorbing species, each of which generates a primary photoproduct. Consistent with the apparent absence of Meta-R_y formation during Lumi-O_f decay, we postulated that only the red-absorbing species leads to photoproduct. This model estimated a Lumi-R_f species-associated difference spectrum (SADS) nearly identical to the equivalent SADS estimated from the primary data (38) and to the cryo-trapped intermediate (Fig. S5*F*), predicted a Lumi-O_f SADS that strongly resembles the 10-ns minus 2-ns spectrum (Fig. S5*E*), and accurately described biphasic decay of absorbance at 680 nm (Fig. S5*C*). Taken together, these results confirm the presence of an orange-absorbing population in the dark state of wild-type NpR0612g4 and demonstrate that this population does not undergo full photoconversion.

Asp657 and Photochemical Heterogeneity. The behavior of the W_{655}A and W_{655}V variants implicates a correlation between the Trp-out population and the orange-absorbing species in the wild-type NpR6012g4 dark state but does not explain why that population would exhibit orange absorbance. We noted that the Asp657 sidechain adopts a "vertical" orientation in eight out of nine Trp-in structures but a "horizontal" orientation in the Trp-out structure and the ninth Trp-in structure (Fig. 3 *C* and *D*). The vertical Asp side chain makes one hydrogen bond each to the PCB B- and C-ring NH protons and a third to the backbone NH proton of Leu660 (Fig. 3*C*), whereas the horizontal Asp side chain makes one hydrogen bond each to the backbone NH protons of His659 and Leu660 and does not hydrogen bond to PCB (Fig. 3*D*). Two conformations are also seen for Asp657 in the photoproduct (Fig. S3 *H* and *I*), but these differences do not result in complete loss of hydrogen bonding to the B- and C-rings in the photoproduct state. The horizontal Asp orientation in the dark state results in such a loss, with no obvious counterion for the cationic bilin π system. This environment could lead to orange absorption in the dark state either via chromophore deprotonation or via altered electron density in the absence of hydrogen bonding.

Asp657 is not amenable to site-directed mutagenesis (15), and mutagenesis of Trp655 could alter the equilibrium between the horizontal and vertical configurations of Asp657 regardless of the bilin protonation state. However, the vertical Asp configuration places the anionic carboxylate close to the cationic bilin ring system, whereas the horizontal configuration does not. Therefore, protonation of the Asp side chain would be expected to destabilize the vertical configuration relative to the horizontal configuration by weakening this electrostatic interaction. Deprotonation of the chromophore would also have a similar effect, but deprotonation of PCB and protonation of Asp657 would occur under opposite pH conditions: low pH would suppress the orange-absorbing population were deprotonation of PCB to be the cause for orange absorption but would increase that population were protonation of Asp657 to be the cause.

We therefore examined pH effects both in wild-type NpR6012g4 and in Trp655 variants. Absorption spectroscopy of W_{655}V and W_{655}A NpR6012g4 clearly demonstrated decreasing red absorbance and increasing orange absorbance at pH 5 compared with pH 8 (Fig. S4 *C* and *D*). Similarly, red absorbance is decreased at low pH in wild-type NpR6012g4, whereas fluorescence from the orange-absorbing population is increased (Fig. 4*B*). We therefore conclude that the orange-absorbing population of NpR6012g4 is favored by protonation rather than deprotonation and cannot be assigned to chromophore deprotonation.

Discussion

We report solution structures of NpR6012g4 in both photostates. The photoproduct state resembles that recently determined for the red/green CBCR slr1393g3 from *Synechocystis* sp. strain PCC 6803 (PDB ID code 5M82). In both cases, the 15*E* chromophore adopts a twisted geometry at both the C5 and C15 methine bridges, and this twisted geometry seems the likely cause of the blue-shifted photoproduct absorption seen in this CBCR subfamily. Within the calculated ensemble of structures for the dark state, we observe multiple configurations for Trp655 and Asp657, two residues known to play key roles in chromophorylation and spectral tuning (15). Structural heterogeneity of the equivalent Trp residue in AnPixJg2 has been reported in a simulation, but the crystal structure of the AnPixJg2 dark state only contains the Trp-in conformation (34, 49). We also observe a horizontal configuration for the Asp657 side chain that ablates hydrogen bonding to the chromophore B- and C-rings. Substitution of Trp655 results in variant proteins that accumulate varying amounts of an orange-absorbing 15*Z* population (spectral heterogeneity), and we demonstrate the presence of a similar population in wild-type NpR6012g4.

We propose that orange absorption arises due to the horizontal Asp configuration. This minority configuration disrupts hydrogen bonding to PCB, which could cause a spectral shift either via formation of a deprotonated bilin π system (51) or via loss of hydrogen bonding to a protonated π system. Orange-absorbing species increase at low pH both in wild-type NpR6012g4 and in variants with substitutions at Trp655 (Fig. 4*B* and Fig. S4 *C* and *D*), demonstrating that the orange-absorbing species does not arise due to deprotonation of the bilin π system. We propose that structural heterogeneity at Trp655 or substitutions for this residue alter the equilibrium between the two configurations of Asp657. We propose that the vertical Asp orientation still occurs with lower occupancy in such variants, explaining the persistence of red-absorbing species. Similarly, the observed pH effects would be explained were the horizontal configuration to be favored by protonation of a titratable group at low pH. The orange-absorbing species exhibited primary photoisomerization but not full photoconversion, indicating that this species may be photochemically inactive in other red/green CBCRs as well. Our studies thus provide a plausible explanation for the 10-fold observed variation in forward quantum yield for these proteins (39), which impacts development of CBCRs for synthetic biology (52–54).

Our work underscores the value of multiple, complementary approaches in structural characterization of photoproteins. Spectroscopic and photochemical heterogeneity is well established in phytochromes and in CBCRs such as RcaE and NpR6012g4 (13, 14, 16, 17, 19–21, 36–39, 51, 55), but connecting this behavior to structural heterogeneity has proven difficult. Using solution NMR structures, we present evidence that even conserved residues proximal to the chromophore can exhibit structural heterogeneity and link that heterogeneity to specific effects in light perception and photochemistry. We anticipate that similar effects connect structural, spectral, and photochemical heterogeneity in other photoreceptor families (56–58). Indeed, photoreceptors and other signaling "input" domains need to be able to switch between two configurations to regulate signaling; this may make them uniquely suited to the study of structural heterogeneity and its functional consequences.

Materials and Methods

Details are described in *SI Materials and Methods*. This includes information on expression and purification of NpR6012g4, structure determination, and spectroscopic techniques. The PDB ID codes for this work are 6BHN (dark state) and 6BHO (photoproduct).

ACKNOWLEDGMENTS. We thank Rei Narikawa and Wolfgang Gärtner for helpful discussions. This work was supported by Chemical Sciences, Geosciences, and Biosciences Division, Office of Basic Energy Sciences, Office of Science, US Department of Energy Grant DE-FG02-09ER16117 (to J.C.L., D.S.L., and J.B.A.) and NIH Grant R01-EY012347 (to J.B.A.).

1. Ort DR, et al. (2015) Redesigning photosynthesis to sustainably meet global food and bioenergy demand. *Proc Natl Acad Sci USA* 112:8529–8536.
2. Casal JJ (2013) Photoreceptor signaling networks in plant responses to shade. *Annu Rev Plant Biol* 64:403–427.
3. Rockwell NC, Su YS, Lagarias JC (2006) Phytochrome structure and signaling mechanisms. *Annu Rev Plant Biol* 57:837–858.
4. Hu W, Su YS, Lagarias JC (2009) A light-independent allele of phytochrome B faithfully recapitulates photomorphogenic transcriptional networks. *Mol Plant* 2:166–182.
5. Franklin KA, Quail PH (2010) Phytochrome functions in *Arabidopsis* development. *J Exp Bot* 61:11–24.
6. Rockwell NC, Lagarias JC (2010) A brief history of phytochromes. *ChemPhysChem* 11: 1172–1180.
7. Rockwell NC, Lagarias JC (2017) Phytochrome diversification in cyanobacteria and eukaryotic algae. *Curr Opin Plant Biol* 37:87–93.
8. Wagner JR, Brunzelle JS, Forest KT, Vierstra RD (2005) A light-sensing knot revealed by the structure of the chromophore-binding domain of phytochrome. *Nature* 438: 325–331.
9. Essen LO, Mailliet J, Hughes J (2008) The structure of a complete phytochrome sensory module in the Pr ground state. *Proc Natl Acad Sci USA* 105:14709–14714.
10. Yang X, Kuk J, Moffat K (2008) Crystal structure of *Pseudomonas aeruginosa* bacteriophytochrome: Photoconversion and signal transduction. *Proc Natl Acad Sci USA* 105:14715–14720.
11. Burgie ES, Bussell AN, Walker JM, Dubiel K, Vierstra RD (2014) Crystal structure of the photosensing module from a red/far-red light-absorbing plant phytochrome. *Proc Natl Acad Sci USA* 111:10179–10184.
12. Kim PW, et al. (2013) Unraveling the primary isomerization dynamics in cyanobacterial phytochrome Cph1 with multi-pulse manipulations. *J Phys Chem Lett* 4: 2605–2609.
13. Kim PW, Rockwell NC, Martin SS, Lagarias JC, Larsen DS (2014) Heterogeneous photodynamics of the pfr state in the cyanobacterial phytochrome Cph1. *Biochemistry* 53: 4601–4611.
14. Kim PW, Rockwell NC, Martin SS, Lagarias JC, Larsen DS (2014) Dynamic inhomogeneity in the photodynamics of cyanobacterial phytochrome Cph1. *Biochemistry* 53:2818–2826.
15. Rockwell NC, Martin SS, Gulevich AG, Lagarias JC (2014) Conserved phenylalanine residues are required for blue-shifting of cyanobacteriochrome photoproducts. *Biochemistry* 53:3118–3130.
16. Wagner JR, Zhang J, Brunzelle JS, Vierstra RD, Forest KT (2007) High resolution structure of Deinococcus bacteriophytochrome yields new insights into phytochrome architecture and evolution. *J Biol Chem* 282:12298–12309.
17. Song C, et al. (2011) Two ground state isoforms and a chromophore D-ring photoflip triggering extensive intramolecular changes in a canonical phytochrome. *Proc Natl Acad Sci USA* 108:3842–3847.
18. Rockwell NC, et al. (2014) Eukaryotic algal phytochromes span the visible spectrum. *Proc Natl Acad Sci USA* 111:3871–3876.
19. Stensitzki T, et al. (2017) Influence of heterogeneity on the ultrafast photoisomerization dynamics of pfr in Cph1 phytochrome. *Photochem Photobiol* 93: 703–712.
20. Velazquez Escobar F, et al. (2017) Protonation-dependent structural heterogeneity in the chromophore binding site of cyanobacterial phytochrome Cph1. *J Phys Chem B* 121:47–57.
21. Sineshchekov VA (2004) Phytochrome A: Functional diversity and polymorphism. *Photochem Photobiol Sci* 3:596–607.
22. Rohmer T, et al. (2008) Light-induced chromophore activity and signal transduction in phytochromes observed by ^{13}C and ^{15}N magic-angle spinning NMR. *Proc Natl Acad Sci USA* 105:15229–15234.
23. Strauss HM, Hughes J, Schmieder P (2005) Heteronuclear solution-state NMR studies of the chromophore in cyanobacterial phytochrome Cph1. *Biochemistry* 44: 8244–8250.
24. Bhaya D, Takahashi A, Grossman AR (2001) Light regulation of type IV pilus-dependent motility by chemosensor-like elements in *Synechocystis* PCC6803. *Proc Natl Acad Sci USA* 98:7540–7545.
25. Kehoe DM, Gutu A (2006) Responding to color: The regulation of complementary chromatic adaptation. *Annu Rev Plant Biol* 57:127–150.
26. Ikeuchi M, Ishizuka T (2008) Cyanobacteriochromes: A new superfamily of tetrapyrrole-binding photoreceptors in cyanobacteria. *Photochem Photobiol Sci* 7:1159–1167.
27. Enomoto G, Ni-Ni-Win, Narikawa R, Ikeuchi M (2015) Three cyanobacteriochromes work together to form a light color-sensitive input system for c-di-GMP signaling of cell aggregation. *Proc Natl Acad Sci USA* 112:8082–8087.
28. Rockwell NC, Martin SS, Feoktistova K, Lagarias JC (2011) Diverse two-cysteine photocycles in phytochromes and cyanobacteriochromes. *Proc Natl Acad Sci USA* 108: 11854–11859.
29. Rockwell NC, Martin SS, Lagarias JC (2012) Red/green cyanobacteriochromes: Sensors of color and power. *Biochemistry* 51:9667–9677.
30. Fushimi K, et al. (2016) Cyanobacteriochrome photoreceptors lacking the canonical Cys residue. *Biochemistry* 55:6981–6995.
31. Rockwell NC, Martin SS, Lagarias JC (2016) Identification of cyanobacteriochromes detecting far-red light. *Biochemistry* 55:3907–3919.
32. Narikawa R, Fukushima Y, Ishizuka T, Itoh S, Ikeuchi M (2008) A novel photoactive GAF domain of cyanobacteriochrome AnPixJ that shows reversible green/red photoconversion. *J Mol Biol* 380:844–855.
33. Xu XL, et al. (2014) Combined mutagenesis and kinetics characterization of the bilin-binding GAF domain of the protein Slr1393 from the cyanobacterium *Synechocystis* PCC6803. *ChemBioChem* 15:1190–1199.
34. Narikawa R, et al. (2013) Structures of cyanobacteriochromes from phototaxis regulators AnPixJ and TePixJ reveal general and specific photoconversion mechanism. *Proc Natl Acad Sci USA* 110:918–923.
35. Rockwell NC, Martin SS, Lagarias JC (2017) There and back again: Loss and reacquisition of two-Cys photocycles in cyanobacteriochromes. *Photochem Photobiol* 93:741–754.
36. Kim PW, et al. (2012) Second-chance initiation dynamics of the cyanobacterial photocycle in the NpR6012 GAF4 domain of *Nostoc punctiforme*. *J Am Chem Soc* 134: 130–133.
37. Kim PW, et al. (2012) Femtosecond photodynamics of the red/green cyanobacteriochrome NpR6012g4 from *Nostoc punctiforme*. 2. Reverse dynamics. *Biochemistry* 51:619–630.
38. Kim PW, et al. (2012) Femtosecond photodynamics of the red/green cyanobacteriochrome NpR6012g4 from Nostoc punctiforme. 1. Forward dynamics. *Biochemistry* 51:608–618.
39. Gottlieb SM, et al. (2015) Conservation and diversity in the primary forward photodynamics of red/green cyanobacteriochromes. *Biochemistry* 54:1028–1042.
40. Rockwell NC, Martin SS, Lim S, Lagarias JC, Ames JB (2015) Characterization of red/green cyanobacteriochrome NpR6012g4 by solution nuclear magnetic resonance spectroscopy: A hydrophobic pocket for the C15-*E*,*anti* chromophore in the photoproduct. *Biochemistry* 54:3772–3783.
41. Rockwell NC, Martin SS, Lim S, Lagarias JC, Ames JB (2015) Characterization of red/green cyanobacteriochrome NpR6012g4 by solution nuclear magnetic resonance spectroscopy: A protonated bilin ring system in both photostates. *Biochemistry* 54: 2581–2600.
42. Lim S, et al. (2016) ^{1}H, ^{13}C, and ^{15}N chemical shift assignments of cyanobacteriochrome NpR6012g4 in the green-absorbing photoproduct state. *Biomol NMR Assign* 10:157–161.
43. Yu Q, et al. (2016) ^{1}H, ^{15}N, and ^{13}C chemical shift assignments of cyanobacteriochrome NpR6012g4 in the red-absorbing dark state. *Biomol NMR Assign* 10: 139–142.
44. Song C, Narikawa R, Ikeuchi M, Gärtner W, Matysik J (2015) Color tuning in red/green cyanobacteriochrome AnPixJ: Photoisomerization at C15 causes an excited-state destabilization. *J Phys Chem B* 119:9688–9695.
45. Song C, et al. (2015) A red/green cyanobacteriochrome sustains its color despite a change in the bilin chromophore's protonation state. *Biochemistry* 54:5839–5848.
46. Tjandra N, Bax A (1997) Direct measurement of distances and angles in biomolecules by NMR in a dilute liquid crystalline medium. *Science* 278:1111–1114.
47. Rockwell NC, Shang L, Martin SS, Lagarias JC (2009) Distinct classes of red/far-red photochemistry within the phytochrome superfamily. *Proc Natl Acad Sci USA* 106: 6123–6127.
48. Yang X, Kuk J, Moffat K (2009) Conformational differences between the Pfr and Pr states in *Pseudomonas aeruginosa* bacteriophytochrome. *Proc Natl Acad Sci USA* 106: 15639–15644.
49. Scarbath-Evers LK, et al. (2017) Structural heterogeneity in a parent ground-state structure of AnPixJg2 revealed by theory and spectroscopy. *Phys Chem Chem Phys* 19: 13882–13894.
50. Gottlieb SM, Corley SC, Madsen D, Larsen DS (2012) Note: A flexible light emitting diode-based broadband transient-absorption spectrometer. *Rev Sci Instrum* 83: 056107.
51. Hirose Y, et al. (2013) Green/red cyanobacteriochromes regulate complementary chromatic acclimation via a protochromic photocycle. *Proc Natl Acad Sci USA* 110: 4974–4979.
52. Tabor JJ, Levskaya A, Voigt CA (2011) Multichromatic control of gene expression in *Escherichia coli*. *J Mol Biol* 405:315–324.
53. Narikawa R, et al. (2015) A biliverdin-binding cyanobacteriochrome from the chlorophyll *d*-bearing cyanobacterium *Acaryochloris marina*. *Sci Rep* 5:7950.
54. Nakajima M, Ferri S, Rögner M, Sode K (2016) Construction of a miniaturized chromatic acclimation sensor from cyanobacteria with reversed response to a light signal. *Sci Rep* 6:37595.
55. Mathes T, et al. (2015) Femto- to microsecond photodynamics of an unusual bacteriophytochrome. *J Phys Chem Lett* 6:239–243.
56. Coureux PD, Fan ZP, Stojanoff V, Genick UK (2008) Picometer-scale conformational heterogeneity separates functional from nonfunctional states of a photoreceptor protein. *Structure* 16:863–872.
57. Alexandre MT, et al. (2009) Primary reactions of the LOV2 domain of phototropin studied with ultrafast mid-infrared spectroscopy and quantum chemistry. *Biophys J* 97:227–237.
58. Alexandre MT, van Grondelle R, Hellingwerf KJ, Kennis JT (2009) Conformational heterogeneity and propagation of structural changes in the LOV2/Jalpha domain from *Avena sativa* phototropin 1 as recorded by temperature-dependent FTIR spectroscopy. *Biophys J* 97:238–247.